Toward optimal performance of systems for digital optical phase conjugation

Pidong Wang,[1,2,*] Senlin Jin,[3] Feng Huang,[1,2] Dong Li,[1,2] Kun Chen,[1,2] Mingle Liao,[1,2] Qian Li,[1,2] and Yao Yao[1,2,†]

[1]*Microsystem and Terahertz Research Center, China Academy of Engineering Physics, Chengdu 610200, China*
[2]*Institute of Electronic Engineering, China Academy of Engineering Physics, Mianyang 621999, China*
[3]*Center for Advanced Measurement Science, National Institute of Metrology, Beijing 100029, China*

Digital optical phase conjugation (DOPC) emerges as a promising technique for controllable optical delivery in strongly scattering media. Notably, due to the long-standing challenges in accurate alignment of the wave-front sensor and spatial light modulator (SLM), conventional DOPC systems heavily rely on digital calibration for misalignments between these two devices, which will significantly increase the pixel crosstalk of the SLM and thus degrade the performance of DOPC systems. To circumvent this digital calibration for mitigation of the pixel crosstalk, here we propose and demonstrate a real-space alignment scheme for DOPC systems based on single-pixel imaging, which enables precise alignment of the SLM and wave-front sensor: (i) with off-plane alignment precision of submillimeter and milliradian for axial and angular positions, respectively, and (ii) with in-plane pixel match at subpixel resolution. With additional efforts on fidelity optimization of optical phase-conjugation, deformations on the phase-conjugated wave front can almost be removed and the DOPC system would exhibit ultrahigh performance, with peak-to-background ratio (PBR) approaching the theoretical limit (more than 90%) in the time-reversed optical refocusing test. It can be anticipated that all DOPC-based applications will tremendously benefit from this near-theoretical-limit performance of optical phase conjugation for improved capacity and practical utility.

I. INTRODUCTION

Manipulating light scattering by wave-front shaping has attracted extensive interest for its ability to overcome the challenge of light transport beyond the optical diffusion limit in random media [1–3], which is promising in deep-tissue *in vivo* biomedical applications (i.e., noninvasive imaging [4,5], phototherapy [6,7], optogenetics [8,9], etc.) and optical communication through the fog, cloud, or disordered multimode fiber [10–12]. Various techniques are actively developed, including feedback-based iterative optimization [2,13,14], transmission matrix approach [15–17], and optical phase conjugation [18–26]. Among them, digital optical phase conjugation (DOPC), also referred to as time reversal and serving as the digital counterpart of analog optical phase conjugation, draws great attention for its ability to focus light against strong scattering with high contrast in short time, since the time-consuming repetitive measurements necessary for iterative optimization and transmission matrix approach are no longer needed

[27,28]. This is advantageous to practical applications of wave-front shaping.

Acting as a phase-conjugate mirror, a DOPC system would generate phase-conjugated light waves, which will trace the original light wave in the backward direction via the time-reversal symmetry [29,30]. The concept of the phase-conjugate mirror is illustrated in Fig. 1. The wave front of an incident beam is distorted by a scattering medium, shown in Fig. 1(a). With an ordinary mirror, as Fig. 1(b) graphs, the scattered light would be reflected following the law of reflection. By comparison, the phase-conjugate mirror, presented in Fig. 1(c), flips the sign of phase of the scattered light, and consequently the reflected beam will propagate along the same light path but in completely opposite direction with respect to the incident light, just like a time-reversed copy of the original light field, which is in sharp contrast to the ordinary mirror. Being a digital version of the phase-conjugate mirror, the DOPC is implemented in two steps: (i) record—recording the wave front of the scattered light by a wave-front sensor; (ii) playback—generating a phase-conjugated copy of the recorded wave front with a wave-front modulator, such as a spatial light modulator (SLM) based on liquid crystal on silicon (LCOS)

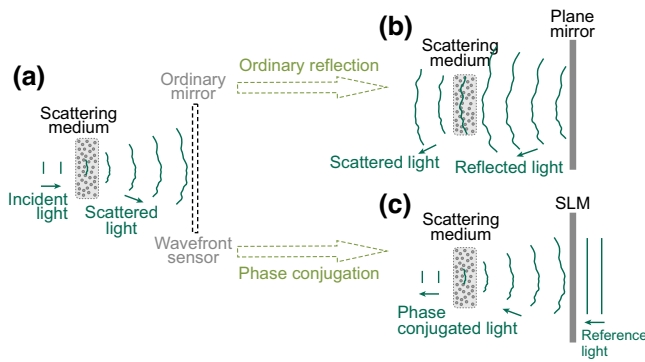*wangpidong_mtrc@caep.cn
†yaoyao_mtrc@caep.cn

FIG. 1. Comparison of optical phase conjugation with the ordinary reflection. (a) Light scattering by the scattering medium and wave-front record of the scattered light by the wave-front sensor. (b) Ordinary reflection of the scattered light with a plane mirror. (c) Time-reversed backpropagation of the phase-conjugated light generated from the reference light with phase modulated by the SLM.

[29–31] or a digital micromirror device (DMD) [19,32] for time-reversed backward propagation.

To ensure that the phase-conjugated copy is a real time reversal of the original scattered light in the DOPC system, the phase-conjugated wave front and its corresponding original scattered wave front should coincide with each other but propagate just in opposite directions [29,30]. However, it is challenging to meet this severe condition: (a) since it is hard to measure the actual positions of the SLM and wave-front sensor of high precision, they are difficult to be precisely situated at the same optical position, and thus there always exist in-plane and off-plane misalignments between them, which would lead to a light path deviation between the phase-conjugated light and its original scattered light [18], and even deform the phase-conjugated wave front; (b) the SLM surface and reference wave front are supposed to be flat in theory, but even high-quality SLMs are not completely flat owing to their manufacturing process (namely the static aberration) [33], and there always exist unknown curvatures on the reference wave front in reality, both of which will distort the phase-conjugated wave front [30]; (c) due to the interpixel gaps of the SLM and the protective glass cover on its surface, part of the light reflected off or transmitting through the SLM will not be phase modulated [34]. The wave-front deformation and distortion and those unmodulated lights will bring down the fidelity of the phase-conjugation, which will also put adverse effect on the DOPC. As a consequence, the performance of the DOPC system might be degraded and even deactivated by these imperfect conditions.

Various optimization methods have been proposed to suppress the negative influence of (a) and (b) [35,36]. All of these methods begin with a roughly aligned DOPC system and then proceed with a digital compensation utilizing the phase-modulation ability of the SLM, rather than

precisely situate the wave-front sensor and the SLM in real space due to the long-standing difficulty of measuring their positions accurately. However, in view of the pixel crosstalk caused by the fringing-field effect [37] and elastic forces [38], there will be obvious fly-back zone errors in the area of 2π phase resets where big phase jumps between adjacent pixels exist (i.e., the gray value 255 change to 0), which will reduce the diffraction efficiency of the SLM [37,39]. As a result, the accuracy of digital phase compensation is tremendously reduced [40]. Unfortunately, this effect was overlooked without further consideration in early works. Besides, the misalignment-induced wave-front deformation of the phase-conjugated light, as well as the unmodulated light directly reflected off the SLM, has never been discussed in detail to date. These ignored problems would be responsible for the degradation of the performance in current DOPC systems. To date, the maximal time-reversed focusing efficiency [namely, peak-to-background ratio (PBR) of a DOPC refocusing light spot, which is the most basic and commonly used parameter to characterize the performance of a DOPC system] reaches only 66% of the theoretical limit, even though digital compensation has been implemented [30]. Therefore, a simple and efficient approach for calibration of the system reducing or even fully eliminating the dependency of digital phase compensation, as well as removing those unmodulated lights, is imperative for perfect-performance DOPC.

It is worth noting that speckle pattern is ubiquitous in the DOPC system. As the speckle pattern varies with the propagation of the scattered light, different translational positions will exhibit distinct speckle patterns, and so do angular positions [41]. Consequently a speckle pattern can be regarded as a fingerprint to mark the optical position of a plane in real space. With this consideration, the optical positions of the SLM and the wave-front sensor could be labeled by the speckle pattern on their surfaces, that is to say, speckle patterns on their surfaces will be the same only on the condition that these two devices share the same optical position. Therefore, if the speckle pattern on the surface of the SLM can be precisely captured, the SLM and the wave-front sensor can be placed at just the same optical position in real space by comparison of the speckle patterns on their surfaces. Fortunately, single-pixel imaging provides a very successful approach to capture images on the surface of the SLM [42,43] and digital speckle correlation (DSC) supplies a powerful tool for the comparison of speckle patterns [44–47]. By this way, we no longer need digital compensations for misalignments of optical positions, and the fly-back zone errors can be reduced. On the other side, since the unmodulated light reflected off or transmitting through the SLM will appear at the 0th diffraction order, optical filtering techniques [34,48] could be adopted to eliminate the adverse effect of the unmodulated light on a DOPC system.

In this work, we pursue optimal performance of a DOPC system. To achieve this goal, a precise real-space alignment scheme is designed based on single-pixel speckle imaging to circumvent conventional digital calibration of the system misalignments for mitigation of the pixel crosstalk. With this scheme, the SLM and wave-front sensor could be accurately settled in real space for optimal alignment of the phase-conjugated wave front: with off-plane axial and angular positions at submillimeter and milliradian levels, respectively, and in-plane pixel match at subpixel accuracy. Moreover, by employing parallel single-pixel imaging, a rapid alignment of the DOPC system of high precision can be implemented even for SLMs with slow response time. With further efforts on improvement of the phase-conjugation fidelity, including digital compensation for curvatures of the reference wave front and surface of the SLM, and elimination of the 0th diffraction order of the SLM by optical filtering, deformations on the phase-conjugated wave front could be reduced to a very low extent and the DOPC system would exhibit an ultra-high performance, approaching the theoretical prediction in the time-reversed refocusing experiment, which would be beneficial to applications of DOPC in both the static and dynamic random media.

II. DOPC SETUP AND METHODOLOGY

In this work, we propose a modified DOPC configuration shown in Fig. 2, in which a SCMOS camera (Thorlabs, CS2100M-USB), together with an electro-optical modulator (EOM), is utilized as a phase-shifting interferometric wave-front sensor [49] for imaging the wave front of the scattered light. And a reflective SLM (Holoeye, PLUTO-VIS-016) is placed in the mirror position of the SCMOS around a beam splitter for generation of the phase-conjugated wave front. A He-Ne laser beam is split into a reference beam and a signal beam. The reference beam is spatially filtered, expanded, and collimated to overfill the full active area of the SLM. The signal beam is expanded by a beam expander and then scattered by a light scattering medium (in this case, three layers of ground glass stacked on top of each other are used, OptoSigma, DFB1-50C02-1500). The scattered light is collected by an objective lens OL and incident on the SLM and the SCMOS. With these two devices, the wave front of the scattered light can be recorded and played back for time reversal. As an essential modification, a single-pixel camera is also constructed in the light path for precise real-space alignment of the DOPC system, which is composed by components in the dashed yellow area. With this camera the speckle pattern on the surface of the SLM can be captured, and then alignment of the DOPC system could be implemented with the aid of the DSC method.

Considering the misalignments and fidelity degradation mentioned in the Introduction, the DOPC system will be
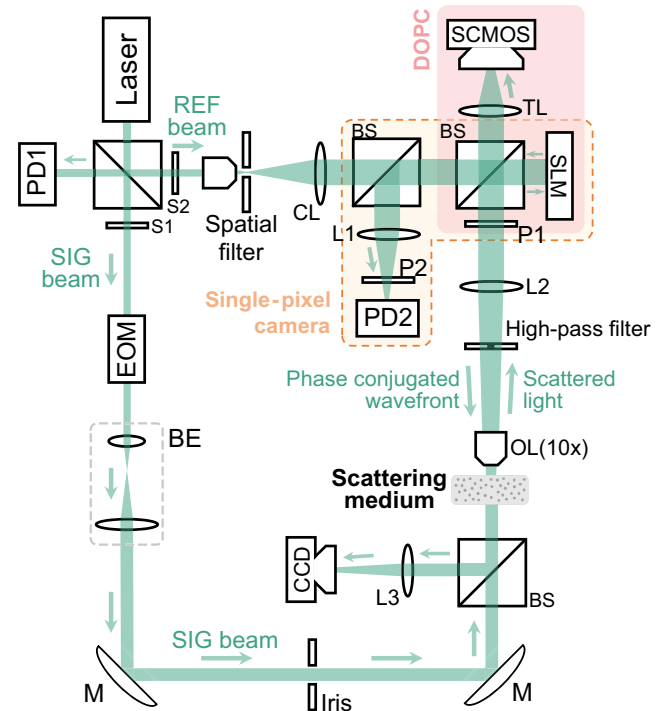

FIG. 2. Schematic of the single-pixel imaging assisted DOPC system. S1 and S2, shutter; PD1 and PD2, photodiode; CL, collimating lens; BS, beam splitter; L1, L2 and L3, lens; P1 and P2, polarizer; TL, telecentric lens; OL, $10\times$ objective lens; EOM, electro-optical modulator; BE, beam expander; M, mirror.

precisely aligned and optimized step by step in the following sections. Figure 3 is a schematic diagram of the whole procedure.

A. Alignment of the SLM and fidelity optimization

To guarantee that the phase-conjugated light would propagate in the exact opposite direction to the original scattered light, the reference beam is always claimed to be at normal incidence to the SLM [18,30,35]. This requirement could be fulfilled by carefully adjusting the tip and tilt angle of the SLM. Figure 4(a) drafts a simplified vignette of the experimental setup relevant to the calibration, where the transmission of the backpropagating light reflected off the SLM through the pinhole of the spatial filter is monitored by a photodiode PD1. We tip and tilt the SLM with two motorized actuators to adjust the incident angle of the reference beam and record the transmitted intensity of the backpropagating light, which is illustrated in Fig. 4(b). When the transmitted intensity reaches its maximum, i.e., the point at the center of the bright spot in Fig. 4(b), the reference beam is at exactly normal incidence to the SLM.

In order to restrain the distortion of the phase-conjugated wave front induced by the curvatures of the SLM surface and reference wave front, digital compensation could be implemented to correct them after the alignment of the
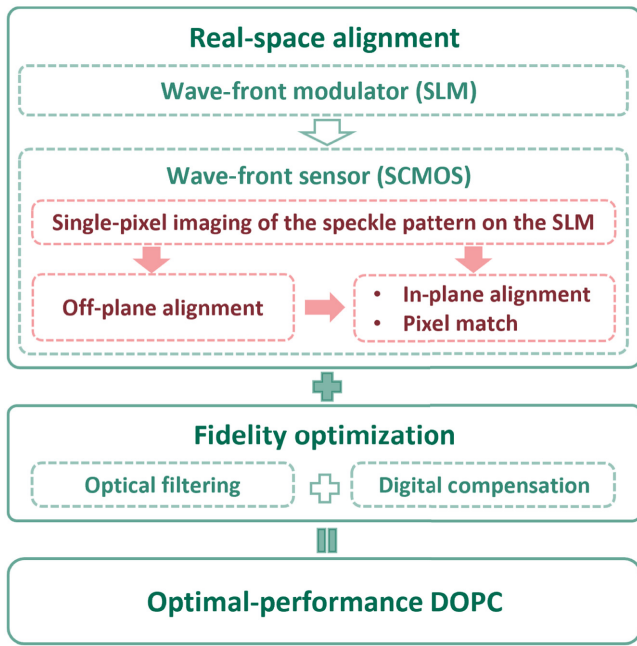
FIG. 3. Schematic diagram for the real-space alignment and optimization of the DOPC system.

SLM. Here we adopt the method in which orthonormal rectangular polynomials, shown in Fig. 4(c), are employed to carry out this correction [35,50]. The key idea of this

method lies in the fact that the phase aberration induced by curvatures of both the reference wave front and the SLM surface could be decomposed into orthonormal rectangular polynomials, thus allowing compensation with a phase pattern conjugating to them. Blue bars in Fig. 4(d) graphs the decomposition coefficient Γ_i of each rectangular polynomial, while the red line plots the intensity variation of the backpropagating light when the phase aberration is compensated by a conjugated-phase pattern including the first i rectangular polynomials. It can be seen that the tilt terms Γ_1 and Γ_2 equal 0, suggesting that the SLM is precisely aligned perpendicular to the incident light by the above method, and consequently, phase compensation for tilt of the SLM is not required and the fly-back zone error is reduced. Figure 4(e) illustrates the final compensation phase pattern. (See Appendix A for details.)

Due to the pixelated structure of the SLM and the protective glass cover on its surface, part of its reflected light is not phase modulated. Optical filtering could be implemented to eliminate their influence. As these unmodulated lights will appear at the 0th diffraction order of the SLM, here a high-pass filter is utilized to filter them out, which is set to the focal plane of lens L2 just after the alignment of the SLM (see Appendix B for details). With the above digital compensation and optical filtering, fidelity of the phase-conjugation could be optimized, whose positive influence would be shown in the following DOPC refocusing experiment.

B. Alignment of the SCMOS to the SLM

In fact, misalignments between the SLM and the wave-front sensor (SCMOS) occur both in plane (i.e., translation and rotation) [30] and off plane (i.e., axial translation, tip and tilt), as shown in Fig. 5(a) where a perspective view
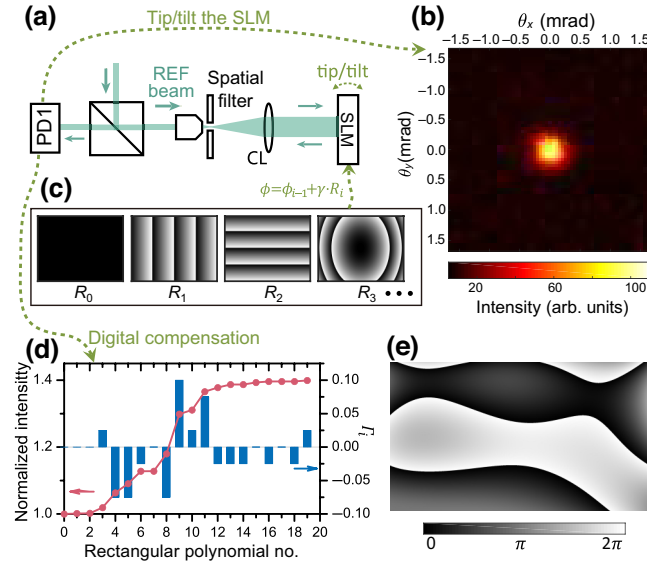

FIG. 4. (a) Experimental setup relevant to the transmission of the backpropagating light reflected off the SLM through the pinhole of the spatial filter, simplified from Fig. 2. (b) Intensity of the transmitted backpropagating light versus the tip and tilt angle of the SLM. (c) The first four orthonormal rectangular polynomials. (d) Compensation coefficient of each rectangular polynomial and the transmitted backpropagating signal. (e) The final compensation phase pattern.

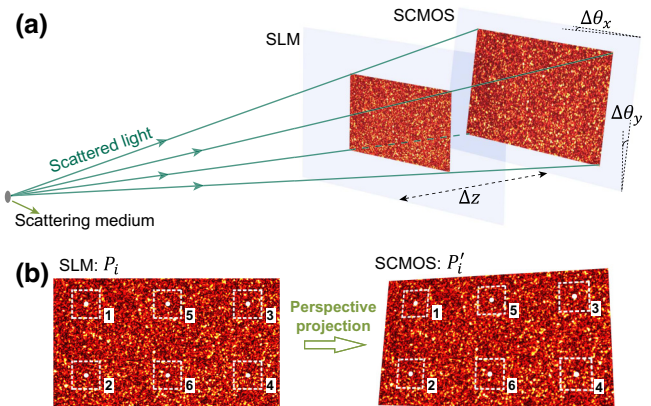FIG. 5. (a) Misalignments between optical positions of the SLM and the wave-front sensor (SCMOS) in perspective view. Axial translation: Δz, tip and tilt: $\Delta\theta_x/\Delta\theta_y$. (b) Perspective projection of a speckle pattern on the SLM onto the SCMOS camera.

of the optical positions of these two devices is illustrated. Mismatch between pixels of these two devices would arise on account of the in-plane misalignment. For off-plane misalignments, it is apparent that the speckle pattern on the SCMOS would be deformed with respect to that on the SLM, and the deformation can be classified into two categories: (i) coherent part, caused by the coherence nature of the scattered light in the view of wave optics, which would change the grain texture of the speckle pattern, and (ii) the noncoherent part, i.e., perspective distortion in the view of geometric optics, which would stretch or skew the speckle pattern without texture variation. Owing to the long-term difficulty in measuring the speckle deformation, especially the coherent deformation, it is hard to fully compensate them with digital methods. This might be part of the main reasons why the time-reversal efficiency is much below the theoretical prediction thus far.

In this work, we leverage the speckle pattern generated by the scattering of the signal beam to precisely locate the actual positions of the SLM and SCMOS camera. Upon this approach, both the minimal in-plane and off-plane misalignments could be pursued for diminishing the speckle-pattern deformation and pixel mismatch, and thus high-quality phase conjugation can be obtained even without any digital calibration for these misalignments. While the SLM has been aligned to be exactly perpendicular to the reference beam in the preceding step, here the SCMOS camera will be adjusted to minimize their misalignments so that they share the same optical position. In this section, the speckle pattern on the SLM will be captured by a single-pixel camera firstly. And then the alignment (including off-plane alignment, in-plane alignment and pixel match) will be implemented individually based on the captured speckle patterns on the SLM and SCMOS camera.

1. Single-pixel imaging of the speckle pattern

As shown in Fig. 2, after being scattered by the scattering medium, the signal beam will illuminate the SLM and the wave-front sensor, and speckle patterns would emerge on their surfaces. A single-pixel camera is built to capture the speckle pattern on the surface of the SLM.

A simplified experimental setup relevant to speckle-pattern imaging on the SLM and the SCMOS camera is illustrated in Fig. 6(a). A photodiode PD2 is utilized to detect the intensity of the light reflected off the SLM for single-pixel imaging of the speckle pattern on its active area. We rotate the polarizers P1 and P2 to be at angles of 45° and −45° from the vertical, respectively, so that the phase-only SLM could control the reflected intensity of the incident light [51,52]. In this work, Hadamard basis shown in Fig. 6(b), is chosen to be the measurement basis for single-pixel imaging. Figure 6(c) plots the intensity fluctuation of the light reflected off the SLM with respect to
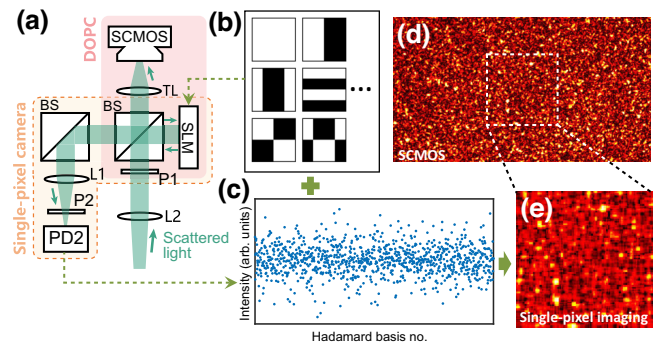

FIG. 6.　(a) Experimental setup relevant to imaging of the speckle patterns on the surface of the SLM and the SCMOS, simplified from Fig. 2. (b) Hadamard basis to be displayed on the SLM. (c) Light intensity reflected off the SLM with respect to the Hadamard basis patterns. (d) Speckle pattern captured by the SCMOS of 1920 × 1080 pixels. (e) Speckle pattern obtained by the SLM-based single-pixel imaging method, of 512 × 512 pixels and at Nyquist sampling rate of 1.25%.

the Hadamard basis sequence, which is detected by the photodiode PD2. Image on the active area of the SLM can be reconstructed from this fluctuation by a single-pixel imaging algorithm [53]:

$$I(\rho) \propto \langle SH(\rho) \rangle - \langle S \rangle \langle H(\rho) \rangle. \qquad (1)$$

Here $I(\rho)$ represents the speckle pattern on the active area of the SLM with ρ being the pixel coordinates on its surface, S is the intensity detected by PD2, and $H(\rho)$ denotes the Hadamard basis. $\langle * \rangle \equiv 1/N \sum_{i=1}^{N} *$ describes an ensemble average over N Hadamard basis patterns.

Figure 6(d) shows a speckle pattern captured by the SCMOS, while Fig. 6(e) presents its counterpart obtained by the single-pixel camera. Taking into consideration the time consumption, here the single-pixel camera only takes advantage of a small part of the SLM and is at Nyquist sampling rate, for instance, Fig. 6(e) is 512 × 512 pixels and at Nyquist sampling rate of 1.25% (that is to say, $N = 1.25\% \times 512^2$, where 512^2 is the total number of Hadamard basis patterns for full sampling rate). The mean speckle size approximates 17.9 times of the SLM's pixel pitch, which is obtained by calculating the width of the normalized autocorrelation function of the speckle pattern [54,55]. It can be seen that the Nyquist sampling indeed degraded the fidelity of a speckle pattern, but its main texture has been retained, and therefore the likeness to its high-quality counterpart captured by the SCMOS can be recognized (see below for more details). According to our experience, for speckle size larger than 10 times of the pixel pitch, the Nyquist sampling is enough to capture the main texture of the speckle pattern. Once the speckle patterns on the surfaces of the SCMOS and the SLM have been obtained, the alignment of these two devices can be implemented by comparing the similarity between them.

2. Off-plane alignment

We mount the wave-front sensor (SCMOS) on an assembled electric moving stage, which can move along z axis and rotate around x and y axis, and hence the off-plane variation of the speckle pattern can be monitored. Meanwhile, the speckle pattern inside an area covering $N \times N$ ($N = 512$ in this work) pixels surrounding the center point of the SLM was captured by the single-pixel camera. Figures 6(d) and 6(e) show an example of speckle patterns acquired in this step.

As is well known, the similarity of two images f and g can be assessed by calculating the correlation coefficient:

$$C(f, g) = \frac{\sum_{ij}(f_{ij} - f_m) \times (g_{ij} - g_m)}{\sqrt{\sum_{ij}(f_{ij} - f_m)^2} \times \sqrt{\sum_{ij}(g_{ij} - g_m)^2}}, \quad (2)$$

where f_{ij} and g_{ij} are intensities at point (x_i, y_j) in the image, f_m and g_m are mean intensities over the whole frame. However, because of the pixel mismatch between the SCMOS and SLM, we cannot directly estimate the similarity by this equation. In this work, we make use of the method of DSC, also called digital image correlation (DIC), which is to match the same speckle points in the reference image and its deformed image by seeking the maximal correlation coefficient [47]. This maximal value of correlation coefficient can be regarded as the similarity measure to assess the likeness between speckle patterns. Obviously, in this case, the similarity measure C_M could be approximated by searching for the maximal value over pixel mismatch, including in-plane amplification, rotation, and translation:

$$C_M = \max_{\Phi, u, v} C[f, g(\Phi, u, v)]. \quad (3)$$

Here f is the speckle pattern obtained by single-pixel imaging. $g(\Phi, u, v)$, which is of the same pixel size as f, is a cropped subset of an amplified and rotated speckle pattern with respect to the raw one captured by the SCMOS. The parameter collection $\Phi = (\alpha_x, \alpha_y, \Delta\theta_z)$, where α_x and α_y are amplification factors along x and y axis, respectively, and $\Delta\theta_z$ denotes the rotation angle around z axis. (u, v) is the cropping position in the raw image and the center point of g. Taking advantage of Eq. (3), the likeness between speckle patterns on the SLM and the SCMOS relative to the movement of the electric moving stage can be monitored.

Figure 7(a) are two typical examples displaying the similarity parameter C_M as a function of the axial translation (z position) of the SCMOS, which are obtained with different speckle patterns (denoted as speckle I and speckle II). It is observed that the maximal correlation coefficients vary with Δz, and at $\Delta z = 0$ mm C_M reach their maximum for both speckle patterns, and thus we conclude that the SCMOS and the SLM share the same axial position at this point. The maximal values of C_M are about
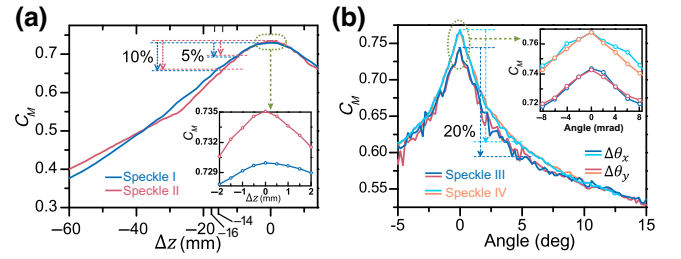

FIG. 7. The maximum correlation coefficient versus (a) Δz, and (b) $\Delta\theta_x$ and $\Delta\theta_y$, for different speckle patterns.

0.73, much smaller than 1. This is caused by the fact that here the single-pixel imaging is only at Nyquist sampling rate, which will degrade the fidelity of the final reconstructed image. However, Fig. 7(a) implies that even such a low image quality will not affect the similarity judgment between two speckle patterns. The minimum step size of the axial translation shown in the inset of Fig. 7(a) is 0.5 mm, and according to our repeated experiments, the peak C_M for different speckle patterns would locate at the same place for such a step size in our system, indicating that the SCMOS could be aligned with an axial distance of submillimeter to the SLM. Figure 7(a) also reveals that an axial translation of 10 mm will only induce a reduction of approximately 5%, and approximately 10% for an axial translation of 16 mm, and consequently, an accuracy of millimeter level is adequate for the axial alignment of the SCMOS camera in most cases, especially for those not perusing perfect performance of the DOPC system.

After the alignment of the axial position, the off-plane angular misalignment will be calibrated. Figure 7(b) graphs the variation of C_M for two typical speckle patterns (denoted as speckle III and speckle IV) versus the tip and tilt angle of the SCMOS with imaging lens TL removed out of the light path, in other words, without any imaging lens in front of the SCMOS camera. This figure unfolds that the similarity parameter drops quickly with the off-plane angular deviation, and a derivation of 5° will result in a drop of approximately 20%, indicating that the speckle pattern is sensitive to the angular derivation of the SCMOS camera, and thus the phase-conjugation fidelity together with the DOPC performance will be considerably influenced by the tip and tilt angle. As shown in the inset of Fig. 7(b), the minimum step size is 2 mrad, and according to our repeated experiments, the peak C_M for different speckle patterns would also locate at the same place for such an angular step size in our system, exhibiting that the angle between the SLM and the SCMOS camera could be reduced to be on the order of milliradian with the proposed method. This will tremendously suppress both the coherent and noncoherent deformation between speckle patterns on these two devices and thus restrain the fidelity reduction of the phase-conjugated wave front to only a few percentage points.

Taking into consideration the size difference between the active area of the SLM and the SCMOS camera, an imaging lens is usually utilized in front of the SCMOS camera to make full use of the active area of these two devices. Due to the tremendous influence of the tip and tilt angle, here a telecentric lens TL (GCO-232203, DHC) is introduced into the light path in front of the SCMOS camera. The numerical aperture (NA) of this lens can reach a minimum value of 0.007 by adjusting the f number with its diaphragm. Thus, only light with an incident angle smaller than about 7 mrad (approximately 0.4°) can transport through this lens and illuminate the active area of the SCMOS, which not only permits precise normal incidence of the reference beam but also enormously eases the alignment of the SCMOS camera. As shown in the inset of Fig. 7(b), only a decrease of about 2.9% occurs for C_M when the SCMOS deviates 7 mrad from the SLM surface, manifesting that the fidelity degradation of the phase-conjugation induced by the tip and tilt angle will be significantly suppressed by this telecentric lens. Furthermore, the active area for the SCMOS is of size about 9.68×5.44 mm, while that of the SLM is about 15.36×8.64 mm. Hence the telecentric lens (magnification factor $\times 0.64$) will enable the SCMOS camera to image the speckle pattern of an almost equal region to the active area of the SLM, which would enhance the utilization rate of pixels on these two devices in the DOPC experiment.

3. In-plane alignment and pixel match

According to Fig. 5(a), speckle patterns on the SLM and the SCMOS are generated by a laser beam scattered from the same scattering medium, and therefore, points on these two speckle patterns could be linked by perspective projection. Thus, the perspective transformation can be used to match pixels on these two devices while also getting rid of the effect of the perspective distortion mentioned above.

Point $P(x, y, z)$ on the surface of the SLM and its projection point $P'(x', y', z')$ on the SCMOS can be related by the following function in homogenous coordinate system [56,57]:

$$\begin{pmatrix} x' \\ y' \\ z' \end{pmatrix} = \begin{pmatrix} a_{11} & a_{12} & a_{13} \\ a_{21} & a_{22} & a_{23} \\ a_{31} & a_{32} & a_{33} \end{pmatrix} \begin{pmatrix} x \\ y \\ z \end{pmatrix}, \quad (4)$$

where a_{ij} ($i, j = 1, 2, 3$) are the elements of the perspective projection matrix. Considering that we could only get access to the two-dimensional pixel coordinates of P and P', it is reasonable to assume that $z = 1$ and $a_{33} = 1$ [56,57], and thus the coordinates of P and P' in two-dimensional Cartesian coordinate system can be denoted as (x, y) and $(X', Y') = (x'/z', y'/z')$, respectively. Therefore, an equation set with Cartesian coordinates can be derived

from Eq. (4):

$$\begin{cases} a_{11}x + a_{12}y + a_{13} - a_{31}xX' - a_{32}yX' = X' \\ a_{21}x + a_{22}y + a_{23} - a_{31}xY' - a_{32}yY' = Y' \end{cases}. \quad (5)$$

As there are eight unknown parameters in Eq. (5), we only need four pairs of projection points, such as P_i and P_i' ($i = 1, 2, 3, 4$) shown in Fig. 5(b), to form eight equations to calculate them. When the perspective projection matrix is acquired, pixels on the SLM and SCMOS can be matched with Eq. (4).

The projection point P_i' of P_i can also be found utilizing the DSC method mentioned in the previous step. If P_i denotes the center point of f, P_i' would be the center point of the cropped subset g, and the coordinates of P_i' (X', Y') could be located by a similar formula to Eq. (3):

$$(\Phi, X', Y') = \arg\max_{\Phi, X', Y'} C\left[f, g\left(\Phi, X', Y'\right)\right]. \quad (6)$$

With methods such as subpixel interpolation, (X', Y') can be found at subpixel resolution [58,59]. To accelerate the single-pixel imaging, a subset of only 150×150 pixels on the SLM is utilized for imaging the speckle pattern and the sampling rate also equals the Nyquist sampling rate in this step.

Figures 8(a)–8(f) show examples of the projection. The blue points mark the positions of the projection point P_i', each of which is of subpixel resolution and acquired with a fully different speckle pattern by moving the scattering medium with a small distance. The red star in the center is the average position of all blue points (60 points) in each subfigure. The light blue circle centering at the red star has radius equaling the pixel pitch of the SCMOS camera (also approximately equaling the pixel pitch of the SLM because of the amplification of the telecentric lens TL). It can be seen that all blue points lie inside the circular area, implying the distances of all blue points from the averaged center are smaller than one pixel pitch. Thus, the point match with DSC method is at pixel level. Furthermore, with the error analysis in Appendix C, it is evident that the averaged projection points (red stars in the center) are of subpixel resolution. Using the averaged coordinates of P_i' ($i = 1, 2, 3, 4$) in Fig. 8, as well as the coordinates of their original point P_i ($i = 1, 2, 3, 4$), the perspective projection matrix can be obtained from Eq. (5), and then the projection relation between the SLM and the SCMOS camera can be evaluated by Eq. (4). Purple crosses in Figs. 8(b) and 8(e) are calculated projection points of P_5 and P_6, namely, P_5' and P_6' in Fig. 5. Depending on the error analysis in Appendix C, the distances between the purple cross and the red star in Figs. 8(b) and 8(e) are about 0.2 and 0.1 times of the pixel pitch, respectively, suggesting that pixel coordinate transformation from the SLM to the SCMOS
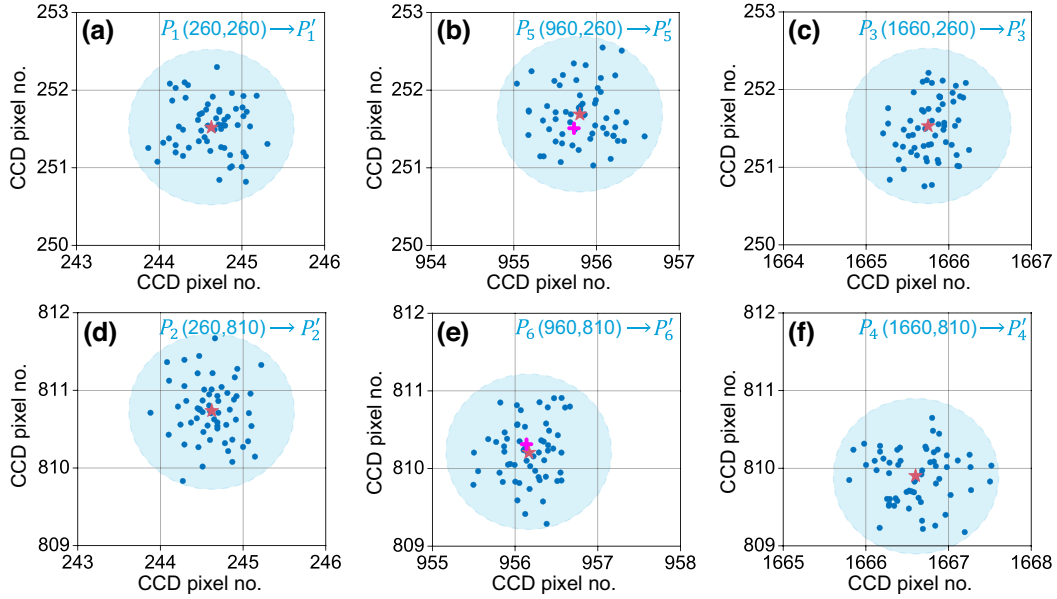
FIG. 8.   Point projection of the original point P_i on the SLM to the projection point P_i' on the SCMOS camera.

is of subpixel resolution with the help of point averaging. The projection points of all other pixels on the SLM could also be calculated in the same way, and thus the high-precision pixel match has been established.

In addition, there always exist in-plane translations and rotations between the SLM and the SCMOS camera, which will reduce their overlap, implying that only a part of their active areas can be utilized for the DOPC experiment. Taking advantage of Eq. (6), the projection points on the SCMOS corresponding to four corners of the SLM could be found, and accordingly, the overlap of these two devices can be evaluated. By in-plane translating and rotating the SCMOS camera, their overlap could be maximized in order to make full use of the active area of these two devices. Finally, with the proposed alignment and pixel match scheme, the SLM and wave-front sensor in the DOPC system could be precisely settled in real space for optimal alignment of the phase-conjugated wave front.

III. DOPC REFOCUSING THROUGH SCATTERING MEDIUM

After the precise alignment of the SLM and the SCMOS in real space, as well as pixel match between these two devices, the conjugated phase of the speckle pattern measured by the SCMOS camera can be mapped to the SLM in the playback stage, and thus the experiment of DOPC refocusing through scattering medium could be performed [10,24]. In our case, the phase of a speckle pattern on the SCMOS camera is measured by the four-step phase-shift method [18,30] after rotating the polarizers P1 and P2 to be in vertical polarizations, and the conjugated phase on the SLM is calculated by two-dimensional interpolation after

the pixel match between the SLM and the SCMOS with the perspective transformation of Eq. (4).

Figures 9(a)–9(c) image the DOPC refocusing light spots imaged by the CCD camera in Fig. 2 when the SLM displays a conjugated phase pattern. Figure 9(a) presents the case with the SLM displaying the raw conjugated phase pattern (denoted as case I). Compared with case I, in Fig. 9(b) an extra phase measured in the step of "digital compensation for the curvatures" is superposed on the conjugated phase (denoted as case II, and see Appendix A for details). Moreover, in Fig. 9(c) the elimination of the 0th diffraction order of the SLM is further considered (denoted as case III, and refer to Appendix B for details). A bright light spot appears in Figs. 9(a)–9(c). In contrast, Figs. 9(d) and 9(e), corresponding to cases without and with the high-pass filter in the light path, respectively, present speckle patterns captured by the CCD camera with each pixel on the SLM randomly and independently modulated, where there is no refocusing light spot observed.

To assess the quality of the refocusing light spot and the performance of the DOPC system, the peak-to-background ratio (PBR, also referred to as intensity enhancement) is adopted, which equals the ratio of the peak intensity of the refocusing light spot to the mean intensity of the background. Because of the high contrast between the peak intensity and the background, as an alternative, the background is usually obtained by measuring the mean intensity of the speckle pattern with a random phase pattern displayed on the SLM [30] (see Appendix E for its theoretical rationale). By theoretical analysis with transmission matrix method, the maximal PBR approximates $\pi N/4$, where N is the number of degrees of freedom controllable by the SLM and the SCMOS camera [21,23]. N is given
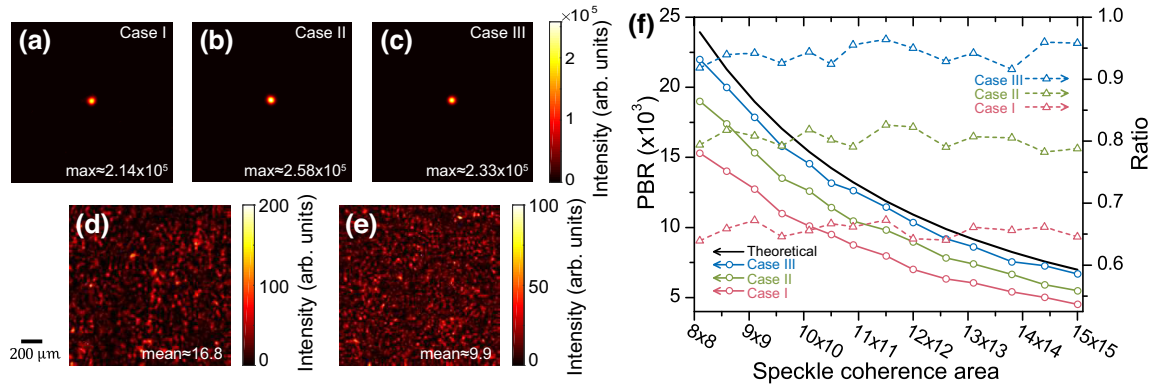
FIG. 9. (a)–(c) A comparison of the refocusing light spot among different occasions: (a) with raw conjugated phase pattern displayed on the SLM (case I), (b) with additional digital compensation superposed (case II), (c) with both digital compensation and high-pass filtering implemented (case III). (d) Speckle pattern captured by the CCD camera with each pixel on the SLM randomly and independently modulated. (e) Similar to (d) except that a high-pass filter is inserted into the light path. (f) PBR of the DOPC refocusing light spot as a function of the speckle coherence area, and the ratio of the experimental PBR to the theoretical prediction: case I, red; case II, green; case III, blue; and the theoretical PBR, black.

by N_p/S where N_p is the total number of effective pixels, S is the speckle coherence area in pixel numbers, namely speckle granularity. In our system, both the SLM and the SCMOS own 1920×1080 pixels, but the pixel pitch of the SCMOS (5.04 μm) is much smaller than that of the SLM (8 μm). In view of the telecentric lens TL ($\times 0.64$), there are only $N_p = 1890 \times 1064$ valid pixels. The speckle coherence area can be evaluated by the aforementioned speckle size of the speckle pattern. The speckle granularity corresponding to Figs. 9(a)–9(c) is around 9.1×9.1 pixels, so the theoretical maximal PBR is about 1.89×10^4. The experimental PBRs corresponding to Figs. 9(a)–9(c) are 1.27×10^4, 1.53×10^4, 1.78×10^4 (see Appendices B and E for details of the PBR evaluation for case III), which achieve about 67%, 81%, and 94% of the theoretical maximum, respectively. Figure 9(f) plots the variation of the PBR to the coherence area of the speckle pattern, which is modulated by modifying the diameter of the incident signal beam with the iris behind the beam expander. The black line is the theoretical maximal PBR $(\pi/4)N_p/S$. The red, green, and blue solid lines are experimental PBRs corresponding to case I, case II, and case III, respectively. In all of the three cases, the PBR declines with the increase of the speckle coherence area, showing a similar tendency to the theoretical formula. The red, green, and blue dashed line plot the ratio of the measured PBR (corresponding to the red, green, and blue solid lines, respectively) to their theoretical maximum, whose average values are around 65%, 80%, and more than 90%, respectively, implying that a relatively high PBR could be acquired if the SLM and the wave-front sensor are well aligned in real space even without any other optimization. And what is more, with further efforts on improvement of the phase-conjugation fidelity according to digital compensation for the curvatures of the reference wave front and SLM surface, accompanied by

optical filtering of the unmodulated light from the SLM, deformations on the phase-conjugated wave front have almost been removed and the time reversal has approached the theoretical prediction. This near-theoretical-limit performance indicates that the real-space alignment method in this work is much more effective, and the influence of pixel crosstalk has been reduced to a very low extent as digital compensation for misalignment is no longer required.

IV. CONCLUSION

In this work, we have presented an efficient scheme for precise real-space alignment of DOPC systems to circumvent conventional digital calibration of the system misalignments. Taking advantage of single-pixel imaging, the speckle pattern on the surface of the SLM has been captured. By comparing the speckle patterns captured by the single-pixel camera and the wave-front sensor with DSC technique, the SLM and wave-front sensor have been precisely aligned in real space: (i) with off-plane axial and angular misalignments at the level of submillimeter and milliradian, respectively, and (ii) with in-plane pixel match at subpixel accuracy. As a consequence, the speckle pattern deformation and pixel mismatch between these two devices have been immensely suppressed, and the coincidence between the phase-conjugated wave front and its original scattered light has been enhanced to a tremendous extent, resulting in the fact that the commonly used digital compensation for misalignment is no longer required and the pixel crosstalk of the SLM has been mitigated. Performing time-reversed optical refocusing in this well-aligned DOPC system, the PBR of the refocusing light spot could reach up to 65% of the theoretical maximal even without any other optimization. Moreover, with parallel single-pixel imaging, quick high-precision alignment

of the DOPC system has been enabled even for SLMs with slow response time (see Appendix D for details).

With additional optimizations on the fidelity of the phase conjugation, including digital compensation for the curvatures of the reference wave front and SLM surface, and elimination of the unmodulated light from the SLM with a high-pass filter, deformations on the phase-conjugated wave front could almost be removed and the PBR could approach the theoretical limit of a DOPC system (more than 90%). It is reasonable to anticipate that the real-space alignment and optimization scheme is also applicable for other DOPC configurations, and the near-theoretical-limit performance of optical phase conjugation is extremely advantageous for DOPC-based applications, such as optical imaging, communication, and manipulation inside or through opaque scattering media.

ACKNOWLEDGMENTS

APPENDIX A: DIGITAL COMPENSATION FOR THE CURVATURES OF THE REFERENCE WAVE FRONT AND SLM SURFACE

To simplify the DOPC playback procedure, the reference beam and the SLM are always required to have a planar wave front and surface, respectively. However, as the reference beam is an expanded Gaussian beam, its wave front is not ideally flat, and furthermore, there always exists surface curvature for commercial SLMs [35]. This unflatness on the reference wave front and SLM surface will distort the phase-conjugated wave front, which would cause a considerable negative influence on the DOPC playback. Fortunately, these imperfections are so small that they could be corrected digitally with a compensation phase pattern displayed on the SLM. Several techniques have been developed to perform this digital correction [30,35,36,60,61].

Here we adopt the method in which orthonormal rectangular polynomials, shown in Fig. 4(c), are employed to carry out this correction [35,50]. The core concept of this method is that the phase aberration induced by curvatures of both the Gaussian wave front and the SLM surface could be decomposed into orthonormal rectangular polynomials, thus allowing compensation with a phase pattern conjugating to them. The backpropagating light, monitored by PD1 in Fig. 2, will be maximized if these two curvatures are fully compensated. Therefore, the main goal of the digital compensation is to seek the proper coefficient of each rectangular polynomial for maximizing the backpropagating signal.

Supposing that the compensation coefficient corresponding to the rectangular polynomial R_i is denoted as Γ_i, the compensation phase consisting of the first $i-1$ rectangular polynomials could be expressed as $\phi_{i-1} = \sum_{j=1}^{i-1} \Gamma_j \times R_j$. To find the value of Γ_i, we multiply the rectangular polynomial R_i by a factor γ and add the product to ϕ_{i-1} to get an alternative phase pattern $\phi = \phi_{i-1} + \gamma \times R_i$. Then we display ϕ on the SLM while simultaneously monitoring the variation of the backpropagating signal by PD1 relative to the value of γ. By scanning γ, the value maximizing the backpropagating signal can be found, which is just the exact value of Γ_i. Thus, the compensation phase pattern composed of the first i rectangular polynomials can be calculated by $\phi_i = \phi_{i-1} + \Gamma_i \times R_i$. The search of Γ_i could be executed one by one starting from $i = 1$ following this route. Only the first 20 rectangular polynomials are exploited in this work, which is sufficient for most occasions. Figure 4(d) plots the decomposition coefficient Γ_i and the intensity variation of the backpropagating light, with respect to the index of the rectangular polynomial. It presents that the intensity will be maximized and tend to be stable after compensating the first 14 rectangular polynomials. Figure 4(e) illustrates the final compensation phase pattern.

APPENDIX B: OPTICAL FILTERING OF THE 0TH DIFFRACTION ORDER OF THE SLM

Here we discuss the filtering of the 0th diffraction order of the SLM in DOPC experiment. Due to the reflection of the protective glass cover and interpixel gaps of the SLM, part of its reflected light is not phase modulated [34,62], which will contribute to the intensity of the background speckle pattern rather than the time-reversed refocusing light spot, and hence the PBR will decrease with respect to the theoretical prediction. Therefore, eliminating the influence of the unmodulated light is essential for high-performance DOPC. We have dealt with this problem in detail in the DOPC experiment.

Since the reflected light without any phase modulation will appear at the 0th diffraction order of the SLM, we can remove their impact by filtering them out with a high-pass filter [34]. In this work, a high-pass filter is set to the focal plane of the lens L2, shown in Fig. 2. Usually, a light filter is a mask with a patterned opaque film on the surface of a glass substrate to block a particular part of the incident light. In consequence, if the filter is only inserted into the light path during the playback stage and removed during the phase record stage, there will be an extra optical path difference induced by the glass substrate between these two stages, which will reduce the PBR provided that this light path difference is not compensated. Besides, the playback stage cannot be implemented synchronously with the phase record stage even if this optical path difference has been compensated, which will affect the real-time performance of the system. Given these facts, the high-pass filter is inserted into the light path at both stages
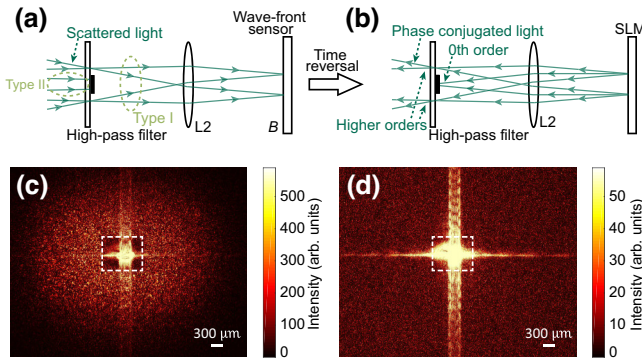
FIG. 10. (a) Light propagation in the phase measurement stage. (b) Filtering out the 0th diffraction order of the SLM during the time-reversal stage. (c) Spatial frequency spectrum of the time-reversed light. (d) Spatial frequency spectrum of the backpropagating light with random phase modulation.

in our experiment, as the simplified vignette displayed in Figs. 10(a) and 10(b).

Figure 10(c) illustrates the spatial frequency spectrum of the time-reversed light in Fig. 9(c), while Fig. 10(d) images that of the backpropagating light in Fig. 9(e) whose phase is randomly modulated by the SLM, both of which are measured at the focal plane of lens L2 where the high-pass filter is placed. It is observed that in both cases light of the 0th diffraction order locates at the center of the image while with those of higher diffraction orders surrounded. In Fig. 10(c), the spatial distribution of the scattering light on the focal plane is reconstructed by the phase-conjugated light, in which an intensity valley appears around the 0th diffraction order, namely the white dashed area in Fig. 10(c). This intensity valley is caused by the squared opaque region on the high-pass filter, which blocks light scattering from the scattering medium to the SLM and the wave-front sensor during the phase record stage, just as shown in Fig. 10(a). Consequently, the phase-conjugated light will bypass this opaque region rather than incident on it. Hence the squared opaque region would merely filter out energy lying inside the white dashed area, i.e., energy of the 0th diffraction order only, just as Fig. 10(b) illustrates. As a consequence, there will be no energy loss for the backpropagating light of the true phase-conjugated part.

Comparing Fig. 9(b) with Fig. 9(a), the peak intensity of the refocusing spot increased about 20%, suggesting that the curvatures of the reference wave front together with the SLM are well compensated. However, the peak intensity in Fig. 9(c) decreases to about 90% of that in Fig. 9(b), which approximates the transmittance of the quartz glass substrate of the high-pass filter, implying that the curvatures of the reference wave front and the SLM are also well compensated in this case, and the decrease of the peak intensity is induced by the reflection of the glass substrate of the high-pass filter. Therefore, except for the reflection of its glass substrate, the high-pass filter will neither enhance

nor reduce the peak intensity of the refocusing light spot. This is consistent with the analysis of Fig. 10(c) in the above paragraph. Considering that light of the 0th diffraction order has been filtered out in Fig. 9(c), its background intensity will be much weaker and the PBR will be much larger than that in Fig. 9(b).

It is worth noting that the the background intensities in Figs. 9(a) and 9(b) are obtained, as an alternative, by measuring the mean intensity of the speckle pattern with a random phase displayed on the SLM. However, if this idea is adopted for Fig. 9(c), fake PBR might appear, since the backpropagating light with random phase modulation is somewhat different for case III. It is evident that the energy in Fig. 10(d) is less concentrated relative to Fig. 10(c), which is caused by the fact that the maximum spatial frequency of the random backpropagating light equals the reciprocal of the SLM's pixel pitch while that of the time-reversed light equals to the reciprocal of the speckle grain size. In addition, there is no dark space inside the white dashed area in Fig. 10(d) while there is an intensity valley for the time-reversed light in Fig. 10(c), indicating that part of the light energy of higher diffraction orders will also be filtered out. As a result, the average intensity for the speckle pattern of random phase modulation will be lowered, consistent with the observation in Fig. 9(e), which is only about 59% of the mean intensity in Fig. 9(d), much smaller than the transmittance of the quartz glass substrate of the high-pass filter. This will lead to a disastrous consequence: the measured PBR will be exaggerated, sometimes even greater than the theoretical prediction.

To solve this problem, the size of the opaque region on the high-pass filter should be precisely equal to the size of the 0th diffraction order of the SLM, to guarantee that only light of the 0th diffraction order would be filtered out. However, we may not have a high-pass filter of proper size in hand. In this situation, there is also a simple expedient way to solve the problem if a high-pass filter of a larger size is used. The spatial frequency spectrum in Fig. 10(c) indicates that the time-reversed refocusing light spot in Fig. 9(c) is induced by the phase-conjugated light of total energy $E_t \times (1 - \gamma_0) \times t$, where E_t is the total energy of the reference beam incident on the SLM, γ_0 is the proportion of light of the 0th diffraction order, and t is the transmittance of the quartz glass substrate. In contrast, Fig. 10(d) presents that the speckle pattern in Fig. 9(e) is caused by randomly modulated light of total energy $E_t \times (1 - \gamma_0 - \gamma_h) \times t$, where γ_h is the energy loss rate of higher diffraction orders. Hence the actual mean background I_b should be $I_m \times (1 - \gamma_0)/(1 - \gamma_0 - \gamma_h)$, where I_m is the mean intensity of the speckle pattern in Fig. 9(e). Consequently, the true PBR should be modified as

$$\eta_{\mathrm{PBR}} = \frac{I_{\mathrm{peak}}}{I_b} = \frac{I_{\mathrm{peak}}}{I_m \times \frac{1-\gamma_0}{1-\gamma_0-\gamma_h}}, \quad \text{(B1)}$$

where I_{peak} is the peak intensity of the refocusing light spot. The theoretical derivation of this PBR formula will be detailed in Appendix E.

In this work, we employ the modified formula Eq. (B1) to measure the true PBR of a time-reversed refocusing spot. The size of the 0th diffraction order, namely, the size of the bright spot in Fig. 10(c), is measured to be about 400 μm, while the size of the opaque region on the high-pass filter is around 900 μm, much bigger than that of the 0th diffraction order. Using data in Figs. 9(c) and 9(e), the raw measured PBR (without correction of the energy loss of high diffraction orders) is calculated to be around 1.23 times of the theoretical value, much exaggerated relative to the theoretical prediction. $(1 - \gamma_0) \times t$ and $(1 - \gamma_0 - \gamma_h) \times t$ can be acquired by comparing the energy behind the high-pass filter on occasions with and without the high-pass filter inserted into the light path, respectively. In the case of Fig. 9(c), $(1 - \gamma_0) \times t$ is measured to be 69%, while $(1 - \gamma_0 - \gamma_h) \times t$ is measured to be 53% in Fig. 9(e), so the true PBR is shown to be $1.23 \times 53\% \div 69\% \approx 94\%$ of the theoretical value. All blue circles in Fig. 9 are measured by this method, indicating that they all approach the theoretical value.

APPENDIX C: ERROR ANALYSIS OF PERSPECTIVE TRANSFORMATION

In the ideal case for speckle patterns with good sampling rate such as those captured by commercial CCD or CMOS cameras, it is quite simple to match a point of a reference image in its deformed one at subpixel resolution using the method of DSC. However, because of the long-time consumption, pictures captured by single-pixel imaging are usually undersampled, which will affect its image quality and then influence the error of point match with the DSC method. The random blue points in Fig. 8 show that we cannot accurately locate a point of an undersampled reference image, captured by single-pixel imaging in this case, in a well-sampled SCMOS image even though a subpixel DSC algorithm is utilized. As a consequence, the pixel match with perspective transformation cannot be implemented with a low match error (sometimes even larger than the pixel pitch of the SLM). This mismatch will affect the ultimate performance of the DOPC system. Hence, the sampling rate should be raised to improve the picture quality so as to decrease the pixel match error.

However, owing to the ambient light noise, the noise of the detector, and the intensity fluctuation of the laser light, it is hard to capture the speckle pattern with high quality even if a good sampling rate is adopted. Therefore, in this work, we employ another method, which takes the idea of point averaging: considering the random nature of blue points in Fig. 8, the real position of the projection point on the SCMOS could be approximated by averaging all blue points in each subfigure. As the
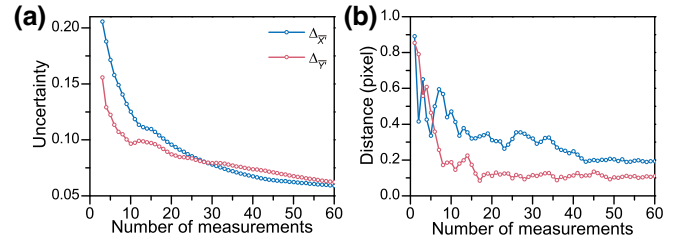

FIG. 11. (a) Uncertainty of the averaged projection point with respect to the number of measurements along *x* (blue) and *y* (red) directions, respectively. (b) Distance between the averaging position of the measured projection points and the calculated one with perspective transformation; the blue and red colors correspond to the distance in Figs. 8(b) and 8(e), respectively.

variance for the average value of a collection of random observations equals the variance of this random collection divided by its size, the true projection point can be approached by increasing the number of blue points, i.e., the number of observations or measurements. The uncertainty of the averaged projection point in Fig. 8(a) is plotted in Fig. 11(a), in which $\Delta_{\overline{X'}}$ and $\Delta_{\overline{Y'}}$ are the uncertainty of $\overline{X'}$ and $\overline{Y'}$, respectively. It can be seen that $\Delta_{\overline{X'}}$ and $\Delta_{\overline{Y'}}$ decrease with the number of measurements, and they get smaller than 0.1 pixels when more than 20 times of measurements are implemented, meaning that 95% of the averaged points will lie inside a square region with a side length of 0.2 pixels around the true projection point. Hence, the averaged projection point is of subpixel resolution. The blue and red lines in Fig. 11(b) graph the distances of the averaging projection points (the red stars) in Figs. 8(b) and 8(e) from the calculated one (the purple crosses) under perspective transformation, respectively, demonstrating that they also decrease with the number of measurements and converge to about 0.2 pixels and 0.1 pixels after 45 measurements. Thus, the random error of the perspective transformation is also under subpixel level. In conclusion, pixel match between pixels on the SLM and the SCMOS camera is of subpixel resolution.

APPENDIX D: FAST SINGLE-PIXEL SPECKLE IMAGING FOR QUICK ALIGNMENT OF THE DOPC SYSTEM

Due to the slow response time for liquid crystal of many commonly used commercial SLMs (for example, 60 ms for the Holoeye PLUTO-VIS-016 used in this work), the imaging frame rate would be severely affected since a picture acquired by single-pixel imaging consists of a large series of measurements, each needing the SLM to display a different measurement basis. In consequence, it is time consuming to align a DOPC system with the proposed scheme. Therefore, improving the frame rate of single-pixel imaging is indispensable for quick alignment of the

DOPC system, especially for SLMs with slow response time.

Fortunately, many algorithms have been put forward to speed up the frame rate, such as single-pixel imaging via comprehensive sensing [63] and deep learning [64]. Here we present a demonstration to improve the frame rate based a simple idea of parallel imaging with a camera array: configure a single-pixel camera array with a single SLM, each capturing the image of a small region on the SLM, and then stitch images obtained by each single-pixel camera to form a large picture. Since each single-pixel camera only needs to image a small region, the number of samples for each camera could be lowered, as well as the sampling time.

In this work, an industrial CCD camera is employed to construct an array of single-pixel detectors for the building of single-pixel camera array. A simplified illustration of the experimental setup relevant to the parallel single-pixel imaging is shown in Fig. 12(a): the single-pixel photodiode PD2 is replaced by an industrial CCD camera, and the collecting lens L1 is replaced by an imaging lens L4. The polarizers P1 and P2 are also 45° and −45° aligned with respect to vertical direction, respectively. The region on the SLM to be imaged is divided into $M \times N$ small subregions, and the CCD camera is employed to detect the reflection of each subregion. An array of $M \times N$ single-pixel cameras could be established for rapid imaging of the speckle pattern as follows:

(1) Calibration of the single-pixel camera array. Firstly the scattering medium is removed from the light path, and the phase pattern of Fig. 12(b) is displayed on the imaging region of SLM. This phase pattern includes $M \times N$

subregions, with the phase of the adjacent subregions alternatively modulated so as to render their images on the CCD to be alternatively bright and dark, as Fig. 12(c) illustrates. Each bright and dark area in Fig. 12(c) can be treated as a superpixel by summing up intensities of all pixels inside this area. Thus the reflection of each subregion on the SLM could be measured by its corresponding superpixel on the CCD camera.

(2) Measurement with Hadamard basis. Reinsert the scattering medium into the light path, and hence the speckle pattern appears on the surface of the SLM. To capture its image, every subregion in Fig. 12(b) displays the Hadamard basis patterns shown in Fig. 12(d) in sequence, and simultaneously the reflection of each subregion is monitored by the corresponding superpixel on the CCD. Figure 12(e) plots intensity fluctuations of four superpixels versus the varying Hadamard basis patterns.

(3) Image reconstruction. Utilizing Eq. (1), the speckle pattern on each of the SLM subregions could be reconstructed. Figure 12(f) graphs the speckle pattern acquired on four subregions corresponding to the intensity fluctuations in Fig. 12(e). By stitching images of all subregions up, the whole speckle pattern could be obtained, such as that shown in Fig. 12(g), which consists of 512×512 pixels (16×16 subregions, and each subregion contains 32×32 pixels) on the SLM imaging area and is at Nyquist sampling rate of about 1.25%.

It is worth noting that the calibration of the single-pixel camera array needs to be performed only once. With this single-pixel camera array, the frame rate is improved $M \times N$ times with respect to the single-pixel camera with only a single detector. For instance, the imaging time of Fig. 12(g)
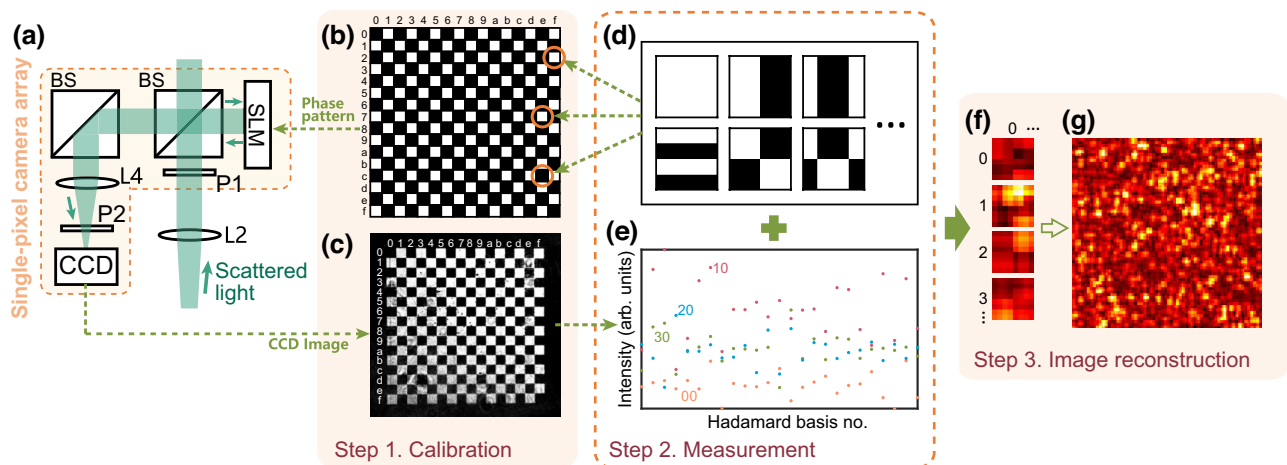

FIG. 12. Parallel imaging of the speckle pattern with a single-pixel camera array. (a) Experimental setup of the single-pixel camera array. (b) Subregions to be imaged on the SLM. (c) Image of the subregions captured by the CCD camera. (d) Hadamard basis to be displayed on each subregion of the SLM. (e) Light intensity reflected off subregions (00, 10, 20, and 30) on the SLM with respect to the Hadamard basis, detected by the corresponding CCD superpixels of 00, 10, 20 and 30. (f) Speckle patterns on subregions (00, 10, 20, and 30) of the SLM acquired by the single-pixel camera array. (g) Full speckle pattern stitched from (f).

is about 2 s, which is only about $1/(16)^2 \approx 0.004$ of the time consumed with a single photodiode detector to capture the same image. Consequently, the time consumption for the entire alignment of the DOPC system could be reduced to a few minutes. Furthermore, if one does not pursue perfect performance in DOPC experiment, averaging is unnecessary for point projection between speckle patterns captured by the single-pixel camera and the wave-front sensor, namely one shot is sufficient. As a result, the alignment procedure could be finished on the order of tens of seconds. With continuing increase of the number of single-pixel cameras in the camera array, the time consumption could be reduced further. Therefore, with the proposed single-pixel imaging-based scheme, quick high-precision alignment of a DOPC system can be implemented even for an SLM with a slow response time.

APPENDIX E: MEASUREMENT OF THE PBR

Since the DOPC refocusing light spot is commonly used to characterize the basic time-reversal performance of a DOPC system, we follow this convention and test the PBR of this refocusing light spot in this work. The PBR is given by $\eta_{\mathrm{PBR}} = I_{\mathrm{peak}}/I_b$, where I_{peak} is the peak intensity of the refocusing light spot and I_b is the mean intensity of the background. The simplest way to get PBR is to measure I_{peak} and I_b directly with a camera. However, it is hard to do so in an actual experiment, because the intensity contrast between I_{peak} and I_b is so high that the commonly used cameras could not obtain them at the same time for their small dynamic range. To solve this problem, an alternative way is proposed, in which I_{peak} is measured directly (at this time, the background intensity approaches zero) but I_b is measured indirectly with the SLM displaying a random phase pattern. This has been widely adopted in previous works about DOPC. By following the theoretical framework of transmission matrix method [21,23], here we will demonstrate analytically that this method could be used not only in conventional DOPC systems, but also in our modified one.

In conventional DOPC systems, namely without elimination of the 0th diffraction order of the SLM with a high-pass filter. As presented in Fig. 13, we describe the input modes on the input plane A of the random medium as a vector $\mathbf{E}^A$ (with elements denoted as $E_m^A, m = 1, 2, \ldots, M$), and $\mathbf{E}^B$ the output modes on the output plane B (with elements $E_n^B, n = 1, 2, \ldots, N$). The transformation of $\mathbf{E}^A$ and $\mathbf{E}^B$ can be described as

$$\mathbf{E}^B = \mathbf{T}^{AB}\mathbf{E}^A, \tag{E1}$$

where $\mathbf{T}^{AB}$ (with elements t_{mn}^{AB}) is the transmission matrix describing the propagation of $\mathbf{E}^A$ from plane A to B. In the playback stage, a phase-conjugated wave front could be
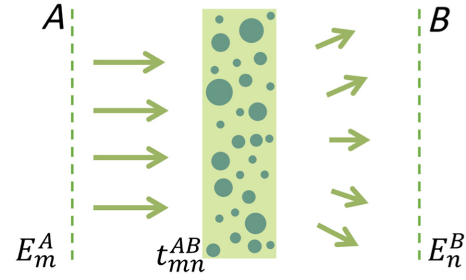

FIG. 13.   Light propagation through the random medium.

obtained on the input plane A:

$$\mathbf{E}^{A'} = \mathbf{T}^{BA}(\mathbf{E}^B)^* = \mathbf{T}^{BA}(\mathbf{T}^{AB}\mathbf{E}^A)^* = (\mathbf{E}^A)^* \tag{E2}$$

$\mathbf{T}^{AB}$ is unitary in perfect phase conjugation, namely $(\mathbf{T}^{AB})^\dagger = (\mathbf{T}^{AB})^{-1} = (\mathbf{T}^{BA})^*$.

However, $\mathbf{T}^{AB}$ is only part of the total transmission matrix in practical applications, and therefore the phase-conjugated wave front is not perfect and a background speckle pattern would appear. Here a system with only one nonzero input mode ($E_1^A = 1$, and $E_m^A = 0$ for $m \neq 1$) will be considered for simplicity but without loss of generality. Thus, the output modes could be obtained by

$$E_n^B = \sum_m^M t_{mn}^{AB} \times E_m^A = t_{1n}^{AB} \times E_1^A = t_{1n}^{AB}. \tag{E3}$$

In the recording stage of phase-only DOPC systems, the phase pattern of E_n^B will be recorded, i.e., $\arg(E_n^B) = \arg(t_{1n}^{AB})$. And in the playback stage, a phase-conjugated wave front will be generated by the phase-only SLM. Supposing that the electric field and intensity of the reference beam are denoted as E_R and I_R, respectively. Thus, the phase-conjugated wave front of the nonzero input mode could be described by

$$E_1^{A'} = \sum_n^N t_{n1}^{BA} \times E_R \times \exp[-i \times \arg(t_{1n}^{AB})] = E_R \sum_n^N |t_{1n}^{AB}| \tag{E4a}$$

$$I_1^{A'} = I_R \times [\sum_n^N |t_{1n}^{AB}|]^2. \tag{E4b}$$

The phase-conjugated wave front of those zero input modes will be

$$E_m^{A'} = E_R \sum_n^N t_{nm}^{BA} \times \exp[-i \times \arg(t_{1n}^{AB})], \quad (m \neq 1), \tag{E5a}$$

$$I_m^{A'} = I_R \times \left| \sum_n^N t_{nm}^{BA} \times \exp[-i \times \arg(t_{1n}^{AB})] \right|^2, \quad (m \neq 1).$$

$$(E5b)$$

Apparently, the ensemble average $\langle I_1^{A'} \rangle$ and $\langle I_m^{A'} \rangle$ denote the peak intensity of the refocusing light spot and the background intensity I_b, respectively. The PBR could be acquired by $\eta_{\mathrm{PBR}} = \langle I_1^{A'} \rangle / \langle I_m^{A'} \rangle$.

Now supposing that the SLM displays a uniformly distributed random phase pattern ϕ_n, the resulting electric light field would be

$$E_m^{A''} = E_R \sum_n^N t_{nm}^{BA} \times \exp[-i \times \phi_n] \qquad (E6a)$$

$$I_m^{A''} = I_R \left| \sum_n^N t_{nm}^{BA} \times \exp[-i \times \phi_n] \right|^2 \qquad (E6b)$$

From the statistical properties of the transmission matrix, we know that t_{nm}^{BA} and t_{1n}^{AB} are independent complex random variables, and the phase of t_{1n}^{AB}, namely $\arg(t_{1n}^{AB})$, is also uniformly distributed, which is the same as ϕ_n. We thus obtain that

$$\left\langle \left| \sum_n^N t_{nm}^{BA} \times \exp[-i \times \phi_n] \right|^2 \right\rangle$$

$$= \left\langle \left| \sum_n^N t_{nm}^{BA} \times \exp[-i \times \arg(t_{1n}^{AB})] \right|^2 \right\rangle. \qquad (E7)$$

Consequently,

$$I_b \equiv \langle I_m^{A'} \rangle = \langle I_m^{A''} \rangle. \qquad (E8)$$

That is to say, the mean background intensity of the phase-conjugated light equals the mean intensity of the light field when the SLM displays a uniformly distributed random phase pattern. This is the rationale behind the idea that the random phase modulation on the SLM gives the genuine background value.

In the modified DOPC system of this work in which a high-pass filter is inserted into the light path. As shown in Fig. 10(a), the light path of the scattered light could be divided into two parts: the part bypassing the opaque region of the high-pass filter (namely along path I, which could reach the wave-front sensor) and others blocked by the opaque area (namely along path II, which could not arrive at the wave-front sensor), in sharp contrast to conventional DOPC systems. We use $t_{mn}^{AB_{\mathrm{I}}}$ and $t_{mn}^{AB_{\mathrm{II}}}$ to describe the transmission matrix mapping each of the M input channels to N possible output modes for light along path I and path II, respectively.

Here a system with only one nonzero input mode ($E_1^A = 1$, and $E_m^A = 0$ for $m \neq 1$) will also be considered for simplicity but without loss of generality. The output modes at plane B (namely the surface plane of the wave-front sensor) in Fig. 10(a) can be obtained by

$$E_n^B = E_n^{B_{\mathrm{I}}} + 0 \times E_n^{B_{\mathrm{II}}} = \sum_m^M t_{mn}^{AB_{\mathrm{I}}} \times \alpha_m E_m^A$$

$$+ 0 \times \sum_m^M t_{mn}^{AB_{\mathrm{II}}} \times \beta_m E_m^A$$

$$= \alpha_1 \times t_{1n}^{AB_{\mathrm{I}}} \qquad (E9)$$

$E_n^{B_{\mathrm{I}}}$ and $E_n^{B_{\mathrm{II}}}$ are electric fields of light coming from path I and path II, respectively. $0 \times E_n^{B_{\mathrm{II}}}$ means that these parts of light are blocked by the opaque area of the high-pass filter. α_m, β_m denote the contribution of incident mode m to output mode n along path I and path II, respectively. According to the principle of superposition, $\alpha_m + \beta_m = 1$.

Following a procedure similar to the above conventional case, the phase-conjugated wave front of the nonzero input modes could be obtained by

$$E_1^{A'} = E_R' \times \left\{ \sum_n^N t_{n1}^{BA_{\mathrm{I}}} \times \alpha_n' \times \exp\left[-i \times \arg\left(\alpha_1 t_{1n}^{AB_{\mathrm{I}}} \right) \right] \right.$$

$$\left. + 0 \times \sum_n^N t_{n1}^{BA_{\mathrm{II}}} \times \beta_n' \times \exp\left[-i \times \arg\left(\alpha_1 t_{1n}^{AB_{\mathrm{I}}} \right) \right] \right\}$$

$$= E_R' \times \sum_n^N \alpha_n' \times |t_{1n}^{AB_{\mathrm{I}}}| \exp[-i \arg(\alpha_1)], \qquad (E10a)$$

$$I_1^{A'} = I_R' \times \left[\sum_n^N \alpha_n' \times \left| t_{1n}^{AB_{\mathrm{I}}} \right| \right]^2. \qquad (E10b)$$

And the phase-conjugated wave front of those zero input modes will be

$$E_m^{A'} = E_R' \left\{ \sum_n^N t_{nm}^{BA_{\mathrm{I}}} \times \alpha_n' \times \exp\left[-i \times \arg\left(\alpha_1 t_{1n}^{AB_{\mathrm{I}}} \right) \right] \right.$$

$$\left. + 0 \times \sum_n^N t_{nm}^{BA_{\mathrm{II}}} \times \beta_n' \times \exp\left[-i \times \arg\left(\alpha_1 t_{1n}^{AB_{\mathrm{I}}} \right) \right] \right\}$$

$$= E_R' \times \sum_n^N t_{nm}^{BA_{\mathrm{I}}} \times \alpha_n' \exp\left[-i \times \arg\left(\alpha_1 t_{1n}^{AB_{\mathrm{I}}} \right) \right],$$

$$(m \neq 1) \qquad (E11a)$$

$$I_m^{A'} = I_R' \times \left| \sum_n^N t_{nm}^{BA_{\mathrm{I}}} \times \alpha_n' \exp\left[-i \times \arg\left(t_{1n}^{AB_{\mathrm{I}}} \right) \right] \right|^2,$$

$$(m \neq 1) \qquad (E11b)$$

Where E_R' and I_R' $(= |E_R'|^2)$ are the electric field and intensity of the light which has been modulated by the SLM, respectively. α_n' and β_n' denote the contribution of the output mode n to the input mode m transporting along path I and path II, respectively, and $\alpha_n' + \beta_n' = 1$. Because the light is the phase-conjugated counterpart of E_n^B, α_n' will approximate 1, consequently,

$$I_1^{A'} \approx I_R' \left[\sum_n^N \left| t_{1n}^{AB_\mathrm{I}} \right| \right]^2 \tag{E12a}$$

$$I_m^{A'} \approx I_R' \left| \sum_n^N t_{nm}^{BA_\mathrm{I}} \times \exp\left[-i \times \arg\left(t_{1n}^{AB_\mathrm{I}} \right) \right] \right|^2, \quad (m \neq 1). \tag{E12b}$$

The average intensity of $I_m^{A'}$ will be

$$\langle I_m^{A'} \rangle \approx I_R' \times N \times \mathrm{Var}\left\{ t_{nm}^{BA_\mathrm{I}} \right\}$$
$$\times \mathrm{Var}\left\{ \exp\left[-i \times \arg\left(t_{1n}^{AB_\mathrm{I}} \right) \right] \right\}, \tag{E13}$$

where $\mathrm{Var}\{*\}$ denotes the variance of a random variable.

If the SLM displays a uniformly distributed random phase pattern ϕ_n, the resulting electric light field would be

$$E_m^{A''} = E_R' \left\{ \sum_n^N t_{nm}^{BA_\mathrm{I}} \times \alpha_n'' \times \exp\left[-i \times \phi_n \right] \right.$$
$$\left. + 0 \times \sum_n^N t_{nm}^{BA_\mathrm{II}} \times \beta_n'' \times \exp\left[-i \times \phi_n \right] \right\}$$
$$= E_R' \times \sum_n^N t_{nm}^{BA_\mathrm{I}} \times \alpha_n'' \times \exp[-i \times \phi_n], \quad (m \neq 1) \tag{E14a}$$

$$I_m^{A''} = I_R' \times \left| \sum_n^N t_{nm}^{BA_\mathrm{I}} \times \alpha_n'' \times \exp[-i \times \phi_n] \right|^2, \quad (m \neq 1) \tag{E14b}$$

where α_n'' and β_n'' denote the contribution of the output mode n to the input mode m transporting along path I and path II, respectively, and $\alpha_n'' + \beta_n'' = 1$. The ensemble average intensity will be

$$\langle I_m^{A''} \rangle = I_R' \times N \times \mathrm{Var}\left\{ \alpha_n'' \right\} \times \mathrm{Var}\left(t_{nm}^{BA_\mathrm{I}} \right)$$
$$\times \mathrm{Var}\left\{ \exp\left[-i \times \phi_n \right] \right\}. \tag{E15}$$

Comparing Eq. (E13) with Eq. (E15), the following equation can be obtained:

$$\frac{\langle I_m^{A''} \rangle}{\langle I_m^{A'} \rangle} \approx \frac{I_R' \times \mathrm{Var}\left\{ \alpha_n'' \right\}}{I_R'} = \frac{I_R' \times \left\{ \mathrm{E}[|\alpha_n''|^2] - |\mathrm{E}[\alpha_n'']|^2 \right\}}{I_R'} \tag{E16}$$

where $\mathrm{E}[*]$ represents the expectation of a random variable.

Since ϕ_n is uniformly distributed in the range of $-\pi \sim \pi$, α_n'' will also be uniformly distributed with the mean value equals to 0, namely $\mathrm{E}[\alpha_n''] = 0$. Consequently,

$$\frac{\langle I_m^{A''} \rangle}{\langle I_m^{A'} \rangle} = \frac{I_R' \times \mathrm{E}[|\alpha_n''|^2]}{I_R'} = \frac{I_R''}{I_R'}. \tag{E17}$$

Apparently, I_R' and I_R'' $(= I_R' \times \mathrm{E}[|\alpha_n''|^2])$ represents light intensity of the part bypassing the optical filter. In the experiment, I_R' and I_R'' are proportional to the energies of the reference beam incident on the surface of the scattering medium, which could be given by $E_t \times (1 - \gamma_0) \times t$ and $E_t \times (1 - \gamma_0 - \gamma_h) \times t$, respectively. As mentioned in Appendix B, E_t is the total energy of the reference beam incident on the SLM, and t is the transmittance of the quartz glass substrate of the high-pass filter, and γ_0 is the proportion of light of the 0th diffraction order, and γ_h is the energy loss rate of higher diffraction orders. In consequence,

$$\frac{\langle I_m^{A''} \rangle}{\langle I_m^{A'} \rangle} = \frac{1 - \gamma_0 - \gamma_h}{1 - \gamma_0} \tag{E18a}$$

$$I_b \equiv \langle I_m^{A'} \rangle = \langle I_m^{A''} \rangle \times \frac{1 - \gamma_0}{1 - \gamma_0 - \gamma_h} = I_m \times \frac{1 - \gamma_0}{1 - \gamma_0 - \gamma_h} \tag{E18b}$$

$\langle I_m^{A'} \rangle$ is the actual average background intensity of the phase-conjugated light field, namely I_b. $\langle I_m^{A''} \rangle$ is the measured mean intensity by the camera with a random phase pattern displaying on the SLM, denoted as I_m in the experiment. Therefore, the PBR in the modified DOPC system in this work could be measured with the following formula:

$$\eta_{\mathrm{PBR}} = \frac{\langle I_1^{A'} \rangle}{\langle I_m^{A'} \rangle} = \frac{I_{\mathrm{peak}}}{I_b} = \frac{I_{\mathrm{peak}}}{I_m \times \frac{1-\gamma_0}{1-\gamma_0-\gamma_h}}. \tag{E19}$$

From Eq. (E19), it can be seen that if the high-pass filter only filters out the 0th diffraction order of the SLM (namely the size of the opaque region on the high-pass filter equals the size of the 0th diffraction order of the SLM), $\eta_{\mathrm{PBR}} = I_{\mathrm{peak}}/I_m$. That is to say, in this situation the PBR measurement is the same as that in conventional case. However, if the high-pass filter is of improper size,

the energy loss of higher orders (γ_h) should be considered to avoid fake PBR values when utilizing this alternative measurement method.

————————

[1] J. Cao, Q. Yang, Y. Miao, Y. Li, S. Qiu, Z. Zhu, P. Wang, and Z. Chen, Enhance the delivery of light energy ultra-deep into turbid medium by controlling multiple scattering photons to travel in open channels, Light Sci. Appl. **11,** 108 (2022).

[2] I. M. Vellekoop and A. P. Mosk, Focusing coherent light through opaque strongly scattering media, Opt. Lett. **32,** 2309 (2007).

[3] H. Cao, A. P. Mosk, and S. Rotter, Shaping the propagation of light in complex media, Nat. Phys. **18,** 994 (2022).

[4] J. Bertolotti, E. G. van Putten, C. Blum, A. Lagendijk, W. L. Vos, and A. P. Mosk, Non-invasive imaging through opaque scattering layers, Nature **491,** 232 (2012).

[5] L. Zhu, F. Soldevila, C. Moretti, A. d'Arco, A. Boniface, X. Shao, H. B. de Aguiar, and S. Gigan, Large field-of-view non-invasive imaging through scattering layers using fluctuating random illumination, Nat. Commun. **13,** 1447 (2022).

[6] N. Kotagiri, G. P. Sudlow, W. J. Akers, and S. Achilefu, Breaking the depth dependency of phototherapy with Cerenkov radiation and low-radiance-responsive nanophotosensitizers, Nat. Nanotechnol. **10,** 370 (2015).

[7] F. Wang, H. He, H. Zhuang, X. Xie, Z. Yang, Z. Cai, H. Gu, and J. Zhou, Controlled light field concentration through turbid biological membrane for phototherapy, Biomed. Opt. Express **6,** 2237 (2015).

[8] S. Shoham, Optogenetics meets optical wavefront shaping, Nat. Methods **7,** 798 (2010).

[9] O. Yizhar, L. Fenno, T. Davidson, M. Mogri, and K. Deisseroth, Optogenetics in neural systems, Neuron **71,** 9 (2011).

[10] M. Nixon, O. Katz, E. Small, Y. Bromberg, A. A. Friesem, Y. Silberberg, and N. Davidson, Real-time wavefront shaping through scattering media by all-optical feedback, Nat. Photonics **7,** 919 (2013).

[11] Y. Zhou, B. Braverman, A. Fyffe, R. Zhang, J. Zhao, A. E. Willner, Z. Shi, and R. W. Boyd, High-fidelity spatial mode transmission through a 1-km-long multimode fiber via vectorial time reversal, Nat. Commun. **12,** 1866 (2021).

[12] Y. Luo, S. Yan, H. Li, P. Lai, and Y. Zheng, Towards smart optical focusing: Deep learning-empowered dynamic wavefront shaping through nonstationary scattering media, Photonics Res. **9,** B262 (2021).

[13] P. Lai, L. Wang, J. W. Tay, and L. V. Wang, Photoacoustically guided wavefront shaping for enhanced optical focusing in scattering media, Nat. Photonics **9,** 126 (2015).

[14] I. M. Vellekoop, Feedback-based wavefront shaping, Opt. Express **23,** 12189 (2015).

[15] I. M. Vellekoop and A. P. Mosk, Universal optimal transmission of light through disordered materials, Phys. Rev. Lett. **101,** 120601 (2008).

[16] S. M. Popoff, G. Lerosey, R. Carminati, M. Fink, A. C. Boccara, and S. Gigan, Measuring the transmission matrix in optics: An approach to the study and control of light propagation in disordered media, Phys. Rev. Lett. **104,** 100601 (2010).

[17] S. M. Popoff, G. Lerosey, M. Fink, A. C. Boccara, and S. Gigan, Controlling light through optical disordered media: transmission matrix approach, New J. Phys. **13,** 123021 (2011).

[18] M. Cui and C. Yang, Implementation of a digital optical phase conjugation system and its application to study the robustness of turbidity suppression by phase conjugation, Opt. Express **18,** 3444 (2010).

[19] D. Wang, E. H. Zhou, J. Brake, H. Ruan, M. Jang, and C. Yang, Focusing through dynamic tissue with millisecond digital optical phase conjugation, Optica **2,** 728 (2015).

[20] Y. Liu, C. Ma, Y. Shen, J. Shi, and L. V. Wang, Focusing light inside dynamic scattering media with millisecond digital optical phase conjugation, Optica **4,** 280 (2017).

[21] Y. M. Wang, B. Judkewitz, C. A. DiMarzio, and C. Yang, Deep-tissue focal fluorescence imaging with digitally time-reversed ultrasound-encoded light, Nat. Commun. **3,** 928 (2012).

[22] Z. Yaqoob, D. Psaltis, M. S. Feld, and C. Yang, Optical phase conjugation for turbidity suppression in biological samples, Nat. Photonics **2,** 110 (2008).

[23] Y. Shen, Y. Liu, C. Ma, and L. V. Wang, Sub-Nyquist sampling boosts targeted light transport through opaque scattering media, Optica **4,** 97 (2017).

[24] J. Yang, J. Li, S. He, and L. V. Wang, Angular-spectrum modeling of focusing light inside scattering media by optical phase conjugation, Optica **6,** 250 (2019).

[25] Z. Li, Z. Yu, H. Hui, H. Li, T. Zhong, H. Liu, and P. Lai, Edge enhancement through scattering media enabled by optical wavefront shaping, Photonics Res. **8,** 954 (2020).

[26] M. Jang, C. Yang, and I. M. Vellekoop, Optical phase conjugation with less than a photon per degree of freedom, Phys. Rev. Lett. **118,** 093902 (2017).

[27] C. Ma, F. Zhou, Y. Liu, and L. V. Wang, Single-exposure optical focusing inside scattering media using binarized time-reversed adapted perturbation, Optica **2,** 869 (2015).

[28] L. Liu, W. Liang, Y. Qu, Q. He, R. Shao, C. Ding, and J. Yang, Anti-scattering light focusing with full-polarization digital optical phase conjugation based on digital micromirror devices, Opt. Express **30,** 31614 (2022).

[29] Z. Yu, M. Xia, H. Li, T. Zhong, F. Zhao, H. Deng, Z. Li, D. Li, D. Wang, and P. Lai, Implementation of digital optical phase conjugation with embedded calibration and phase rectification, Sci. Rep. **9,** 1537 (2019).

[30] M. Jang, H. Ruan, H. Zhou, B. Judkewitz, and C. Yang, Method for auto-alignment of digital optical phase conjugation systems based on digital propagation, Opt. Express **22,** 14054 (2014).

[31] Y. Wan, P. Wang, F. Huang, J. Yuan, D. Li, K. Chen, J. Kang, Q. Li, T. Zhang, S. Sun, Z. Qiu, and Y. Yao, Bionic optical physical unclonable functions for authentication and encryption, J. Mater. Chem. C **9,** 13200 (2021).

[32] P. Wang, F. Chen, D. Li, S. Sun, F. Huang, T. Zhang, Q. Li, K. Chen, Y. Wan, X. Leng, and Y. Yao, Authentication of optical physical unclonable functions based on single-pixel detection, Phys. Rev. Appl. **16,** 054025 (2021).

[33] J. D. Schmidt, M. E. Goda, and B. D. Duncan, Aberration production using a high-resolution liquid-crystal spatial light modulator, Appl. Opt. **46,** 2423 (2007).

[34] H. Zhang, J. Xie, J. Liu, and Y. Wang, Elimination of a zero-order beam induced by a pixelated spatial light modulator for holographic projection, Appl. Opt. **48**, 5834 (2009).

[35] M. Azimipour, F. Atry, and R. Pashaie, Calibration of digital optical phase conjugation setups based on orthonormal rectangular polynomials, Appl. Opt. **55**, 2873 (2016).

[36] P. Zhang, Z. Li, L. Han, D. Liu, and J. Zhu, An automatic optimized method for a digital optical phase conjugation system in focusing through scattering media, Appl. Sci. **10**, 8321 (2020).

[37] B. Apter, U. Efron, and E. Bahat-Treidel, On the fringing-field effect in liquid-crystal beam-steering devices, Appl. Opt. **43**, 11 (2004).

[38] M. Persson, D. Engström, and M. Goksör, Reducing the effect of pixel crosstalk in phase only spatial light modulators, Opt. Express **20**, 22334 (2012).

[39] X. Zhou, S. Jia, Z. Lin, H. Zhang, H. Yu, and Y. Zhang, The improvement of the wavefront modulation accuracy of SLMs based on a grayscale segmentation of the phase modulation curve, Opt. Lasers Eng. **158**, 107160 (2022).

[40] S. Yuecheng, L. Hanpeng, Z. Jiayu, and L. Jiawei, Wavefront shaping technology based on digital optical phase conjugation (invited), Infrared Laser Eng. **51**, 20220256 (2022).

[41] J. W. Goodman, *Speckle Phenomena in Optics: Theory and Applications* (Roberts and Company Publishers, Greenwood Village, CO, 2007).

[42] M. P. Edgar, G. M. Gibson, and M. J. Padgett, Principles and prospects for single-pixel imaging, Nat. Photonics **13**, 13 (2019).

[43] G. M. Gibson, S. D. Johnson, and M. J. Padgett, Single-pixel imaging 12 years on: A review, Opt. Express **28**, 28190 (2020).

[44] N. McCormick and J. Lord, Digital image correlation, Mater. Today **13**, 52 (2010).

[45] B. Pan, K. Qian, H. Xie, and A. Asundi, Two-dimensional digital image correlation for in-plane displacement and strain measurement: A review, Meas. Sci. Technol. **20**, 062001 (2009).

[46] B. Pan, Recent progress in digital image correlation, Exp. Mech. **51**, 1223 (2010).

[47] G. Gu, A comparative study of random speckle pattern simulation models in digital image correlation, Optik **126**, 3713 (2015).

[48] J. Li, Q. Song, P. Tankam, and P. Picart, Eliminating zero-order diffraction in the digital holography wavefront reconstruction with adjustable magnification, Proc. SPIE **7848**, 78481Y (2010).

[49] P. de Groot, in *Optical Measurement of Surface Topography*, edited by R. K. Leach (Springer, Berlin, 2011), Chapter 8, p. 167.

[50] V. N. Mahajan and G. Ming Dai, Orthonormal polynomials in wavefront analysis: Analytical solution, J. Opt. Soc. Am. A **24**, 2994 (2007).

[51] K. Lu and B. E. A. Saleh, Complex amplitude reflectance of the liquid crystal light valve, Appl. Opt. **30**, 2354 (1991).

[52] K. Chaen, H. Takahashi, S. Hasegawa, and Y. Hayasaki, Display method with compensation of the spatial frequency response of a liquid crystal spatial light modulator for holographic femtosecond laser processing, Opt. Commun. **280**, 165 (2007).

[53] Y. Bromberg, O. Katz, and Y. Silberberg, Ghost imaging with a single detector, Phys. Rev. A **79**, 053840 (2009).

[54] I. Hamarová, P. Šmíd, P. Horváth, and M. Hrabovský, Methods for determination of mean speckle size in simulated speckle pattern, Meas. Sci. Rev. **14**, 177 (2014).

[55] D. Chicea, Speckle size, intensity and contrast measurement application in micron-size particle concentration assessment, Eur. Phys. J. Appl. Phys. **40**, 305 (2007).

[56] R. Szeliski, *Computer Vision: Algorithms and Applications* (Springer, Berlin, 2010).

[57] Y. Liu, J. Liu, and Y. Ke, A detection and recognition system of pointer meters in substations based on computer vision, Measurement **152**, 107333 (2020).

[58] B. Pan, K. Li, and W. Tong, Fast, robust and accurate digital image correlation calculation without redundant computations, Exp. Mech. **53**, 1277 (2013).

[59] H. Nobach, N. Damaschke, and C. Tropea, High-precision sub-pixel interpolation in particle image velocimetry image processing, Exp. Fluids **39**, 299 (2005).

[60] A. S. Hemphill, Y. Shen, J. Hwang, and L. V. Wang, High-speed alignment optimization of digital optical phase conjugation systems based on autocovariance analysis in conjunction with orthonormal rectangular polynomials, J. Biomed. Opt. **24**, 1 (2018).

[61] Z. Cheng, J. Yang, and L. V. Wang, Intelligently optimized digital optical phase conjugation with particle swarm optimization, Opt. Lett. **45**, 431 (2020).

[62] J. Liang, S.-Y. Wu, F. K. Fatemi, and M. F. Becker, Suppression of the zero-order diffracted beam from a pixelated spatial light modulator by phase compression, Appl. Opt. **51**, 3294 (2012).

[63] M. F. Duarte, M. A. Davenport, D. Takhar, J. N. Laska, T. Sun, K. F. Kelly, and R. G. Baraniuk, Single-pixel imaging via compressive sampling, IEEE Signal Process. Mag. **25**, 83 (2008).

[64] C. F. Higham, R. Murray-Smith, M. J. Padgett, and M. P. Edgar, Deep learning for real-time single-pixel video, Sci. Rep. **8**, 2369 (2018).